

Major element analysis of natural silicates by laser ablation ICP-MS†‡

Munir Humayun,^{*a} Fred A. Davis^b and Marc M. Hirschmann^b

Received 21st January 2010, Accepted 28th April 2010

First published as an Advance Article on the web 25th May 2010

DOI: 10.1039/c001391a

The complete chemical analysis of natural silicates has previously been accomplished only by combining laser ablation ICP-MS with electron microprobe (EMP) analysis to provide complementary information on major element constituents. Here, we present a method for laser ablation ICP-MS analysis of major elements in silicate glasses and minerals that, when applied using a 193 nm laser system coupled to an ICP-MS, provides precision and accuracy comparable to that of EMP techniques. Replicate analyses of USGS glass reference materials BCR-2G and BHVO-2G have internal precision of 1–4%, and are accurate to better than 5%. Further, the LA-ICP-MS method was applied to volume-averaged analysis of a heterogeneous silicate to yield compositions that are more precise than EMP and more accurate for minor elements, particularly MnO.

Introduction

Natural silicates occur either as amorphous glasses, of volcanic or impact origin, or as crystalline minerals and commonly have a large range of elemental substitutions. Natural silicate minerals and glasses are composed chiefly of a small set of elements in the weight percent (% m/m) concentration range that by convention are reported as oxide percents: SiO₂, TiO₂, Al₂O₃, FeO, Fe₂O₃, MnO, MgO, CaO, Na₂O, K₂O, and P₂O₅. For instrumental analytical methods that cannot distinguish between ferric and ferrous iron, iron is reported as total FeO (FeO_T). The principle technique for the *in situ* microanalysis of major elements in natural silicates is the electron microprobe (EMP). EMP is suitable for analyzing elemental compositions down to the level of a few tens of µg/g (0.010 – 0.001 % m/m). For trace elements, the laser ablation inductively coupled plasma mass spectrometry technique is now widely in use with detection limits in the sub-ng/g range.^{1–3} Such trace element determinations routinely include the determination of one or more major elements (*e.g.*, Ca or Si) as an internal standard.^{3,24} It is, however, desirable to analyze major and trace elements on the same spots as this enables proper correlation between abundances of major elements and trace elements. This would be greatly facilitated if LA-ICP-MS could provide accurate and precise major element analysis. This has been an established practice for natural Fe-Ni alloys,^{4,5} but, with notable exceptions,^{30,31} analysis of major elements in silicates has been avoided because many are prone to

significant molecular isobaric interferences (*e.g.*, ³⁹K and ³⁸ArH), high background levels (*e.g.*, ²³Na) and a lack of suitable reference materials for accurate calibration. Recent contributions from this laboratory have shown that non-stoichiometric ablation can be controlled, and that newly available geological glass reference materials⁶ provide better calibrants than transparent NIST SRM glasses.^{7,8}

Geochemical research commonly requires establishing precise correlations between major element variations and minor or trace element variations occurring in silicates and these correlations are compromised if major and trace elements are determined by separate techniques. In some applications, including those for which we developed the present methods, LA-ICP-MS is preferred because the analysis occurs over a comparatively large sample volume compared with EMP which chiefly probes sample surfaces. LA-ICP-MS requires less stringent sample preparation than charged-particle analytical techniques, including EMP and SIMS,¹ where a high polish (<1 µm) and application of a conductive coating is required. Further, numerous LA-ICP-MS instruments are currently available in laboratories that may not have convenient access to EMP. Here, we describe the application of LA-ICP-MS using sector-field mass spectrometry for the complete major element analysis of natural silicate glasses with spot sizes from 20–50 µm. The technique can readily be applied to solid silicates, as was done for simple compositions previously in our laboratory.⁷ Since we developed the analytical protocols described in this paper using low mass resolving power, the techniques we described should be readily applicable to quadrupole ICP-MS instruments, facilitating wide application of these methods to the entire range of available ICP-MS instruments.

Experimental

Synthetic silicate samples were prepared and analyzed for major element composition by electron microprobe (EMP) at the University of Minnesota. The same samples were subsequently analyzed by laser ablation ICP-MS at Florida State University. The synthesis and analytical methods are described below.

^aDepartment of Earth, Ocean, and Atmospheric Sciences, National High Magnetic Field Laboratory, Florida State University, Tallahassee, FL, 32310-4100. E-mail: humayun@magnet.fsu.edu.; Fax: +850-644-0827; Tel: +850-644-1908

^bDepartment of Geology and Geophysics, University of Minnesota, Minneapolis, 108 Pillsbury Hall, MN, 55455, USA. E-mail: davis957@umn.edu; Marc.M.Hirschmann-1@umn.edu.; Fax: +612-625-6698; Tel: +612-625-3819

† This article is part of a themed issue highlighting some of the most recent and significant developments in the area of Sector Field ICP-Mass Spectrometry.

‡ Electronic supplementary information (ESI) available: Table ESI 1: GeoReM preferred values of MPI-DING and USGS glass reference material. See DOI: 10.1039/c001391a

Experimental silicate sample synthesis

Silicate samples were prepared by fusing a powder of mixed reagent oxides for all major elements (excluding P_2O_5) and Cr corresponding to the composition of KLB-1 peridotite.⁹ Nickel was not included. Experiments were performed in a 1/2" end-loaded piston cylinder apparatus at 3 GPa and 1450–1460 °C for 24 hours. Samples were contained in 4 mm external diameter Pt capsules with an inner graphite liner. Samples were quenched from high pressure, high temperature partial melting experiments conducted with powdered mixtures of 20% basalt and 80% garnet peridotite. While at run conditions, silicate melt, coexisting with mantle mineral phases, migrated to the hottest part of the capsule at the top (Figure 1) providing a large melt pool for analysis. After quenching, the capsules yielded a heterogeneous melt pool comprising disequilibrium crystals and possibly glass (Figure 2), and a residue of equilibrium crystals of olivine, orthopyroxene, clinopyroxene, and garnet. The heterogeneous character of the quenched melt required the application of analytical techniques that can provide a compositional average over a large spatial extent in order to retrieve a single composition for the equilibrium melt phase. Individual disequilibrium phases within the quench were too small to be characterized by electron microprobe.

Electron microprobe analysis

Experimental charges were sectioned vertically and mounted on a brass plug in epoxy. The surface of the charge was polished on nylon pads with a series of dry diamond powders to a 1 or 0.25 μm finish. A carbon coat was applied to the non-conductive sample. Imaging and major element analysis were performed using the JXA-8900 electron microprobe (JEOL Ltd., Tokyo, Japan) at the University of Minnesota.

Quantitative analysis of the quenched melt was performed with an accelerating voltage of 15 kV, a current of 10 nA, and a focused spot (<1 μm diameter). Count times for all oxides,

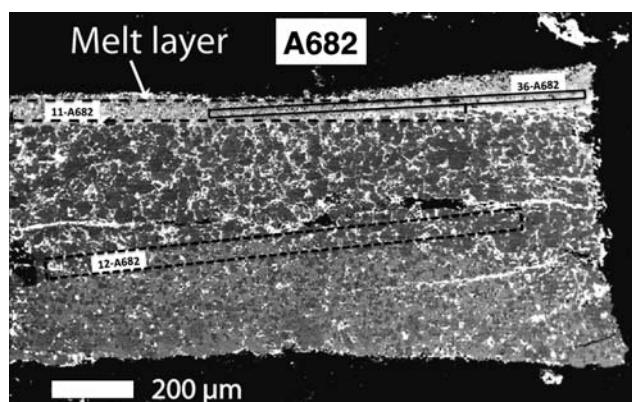


Fig. 1 Back-scattered electron image of experimental sample A682. The silicate sample is contained in a graphite liner (black) inside a Pt capsule (not shown). The melt layer (light gray) migrates to the hottest part of the capsule near the top. Some melt remains distributed throughout the residue. The residue is olivine-rich (dark gray) near the melt layer and pyroxene- and garnet-rich at the base (medium gray). Locations of the three laser ablation tracks (20 μm : solid lines; 50 μm : dashed lines) are marked on the image.

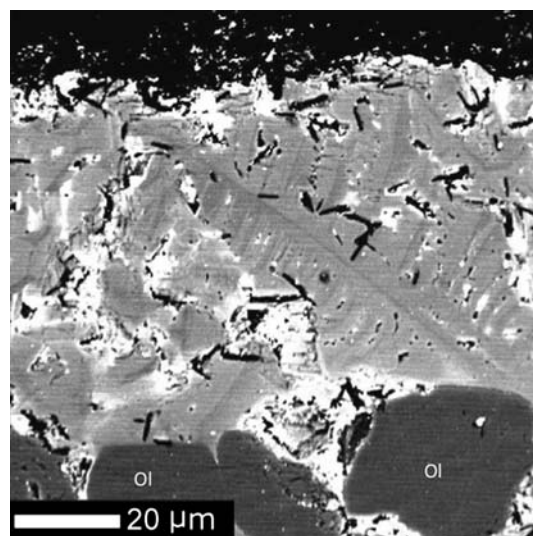


Fig. 2 Back-scattered electron image of experimental sample A682 at higher magnification showing fine structure of the quenched melt region. Quench crystals in the melt (medium gray) form with a dendritic habit. Small elongate holes (black) between the dendrites represent fragile quench products that were difficult to preserve during polish. Residual olivine grains (Ol) are at the base of the melt layer.

except Na_2O , were 10 seconds off peak and 20 seconds on peak. To protect against Na_2O migration, Na_2O count times were 5 seconds off peak and 10 seconds on, and Na_2O was analyzed on the first pass of the spectrometers. Basalt glass and mineral standards were used for calibration and the calibration was checked by analyzing the compositions of two basalt secondary standards (Table 1).

The heterogeneous character of the quenched melt in the experimental charges required collection of many analysis spots (>100) to determine a precise average. Spots were chosen by analyzing along lines with spacing between individual spots of 2–3 μm . Spots chosen in this way avoid collection of a biased set of data, as may result from manual spot selection.

The simple average of spots collected in this way does not give the correct composition of the equilibrium melt phase, because certain fragile quench components are unavoidably lost from the surface during polish (Figure 2). To determine the points that give a representative average a filtering procedure was applied which excluded individual analyses that were not close to Fe-Mg exchange equilibrium¹⁰ with coexisting olivine in the residue. Exchange equilibrium was determined by agreement between

Table 1 List of primary and secondary standards^{26,27} used for electron microprobe analysis of quenched melt and mineral phases

Standard	Element or oxide
Primary Standards:	
Asbestos Microcline ²⁶	K_2O
Indian Ocean Basalt	SiO_2 , Al_2O_3 , FeO^* , MgO , CaO
Kakanui Hornblende	TiO_2 , Na_2O
Mn-Hortonolite	MnO
Tiebaghi Mine Chromite	Cr_2O_3
Secondary standards:	
Indian Ocean Basalt	TiO_2 , Na_2O , K_2O
Makaopuhi basaltic glass	all elements

measured exchange coefficient ($K_D^{\text{Fe-Mg}}$) and model $K_D^{\text{Fe-Mg}}$. By contrast, $K_D^{\text{Fe-Mg}}$ calculated for the unfiltered average is too large to be in equilibrium with the olivine present in the residue of the charge.

Laser ablation ICP-MS analysis

All LA-ICP-MS measurements were performed with a UP 193FX ArF (193 nm) excimer laser ablation system (New Wave™ Research, Fremont, CA, USA) coupled to an Element XR sector-field ICP-MS (Thermo Electron GmbH, Bremen, Germany) at the National High Magnetic Field Laboratory's Plasma Analytical Facility. The sector-field Element XR employs a series of magnetic mass jumps combined with electrostatic scanning to cover the mass spectrum from masses 6–240. The Element XR is equipped with two separate detectors that can be rapidly switched to detect the ion signal from the peak of interest, including an MC-SEV-ICPII (MassCom, Bremen, Germany) dual mode secondary electron multiplier and a Faraday cup, providing a dynamic range from 10^{-1} – 10^{12} cps. The dual mode secondary electron multiplier provides ion counting (0 – 4×10^6 cps) and analog (10^4 – 10^9 cps) modes, while the Faraday cup covers the range 10^7 – 10^{12} cps allowing acquisition of the brightest peaks, including ^{40}Ar ($\leq 2 \times 10^{12}$ cps) and ^{16}O . Daily cross-calibration of the three detector modes was performed by scanning the ^{38}Ar peak over the mass range 37.9–38.1 a.m.u. (200% peak width).

The sample is placed in the UP 193FX ablation cell, and the aerosol produced by ablation is swept into the mass spectrometer using a stream of ultra-high purity He gas (800 ml/min). A stream of Ar gas (~ 900 – 1400 ml/min) is added downstream to achieve the differential flow needed to obtain a bright stable signal, and the flow rate of this gas is tuned for signal optimization on the ICP-MS. A CCD camera allows imaging of the sample during ablation. Spot sizes are controlled by an imaged aperture in the UP 193FX and allow a range from 1–100 μm . In this study, silicate glasses were ablated in line scan mode with spot sizes of 10 μm , 20 μm , and 50 μm , with the sample scanned beneath the laser at rates of 5 $\mu\text{m/s}$ (10–20 μm spots) or 10 $\mu\text{m/s}$ (50 μm spots). The UP 193FX laser has a pulse width of 4 ns, and all analyses were performed with 20 Hz repetition rate and 100% power output (2.5 GW/cm², 12 J/cm²).

All peaks were acquired by peak jumping between peak tops with a 10% mass window and 50 milliseconds of acquisition time on the peak top. The peaks used for each element are given in

Table 2. For the monoisotopic elements Na, Al, P, and Mn, there are no other choices, but for other elements the peak was chosen to limit brightness (^{25}Mg) or to avoid more intense isobaric interferences on the major isotope (^{28}Si , ^{40}Ca , ^{48}Ti , ^{52}Cr , ^{56}Fe , ^{58}Ni). Molecular isobaric interferences originating from gases in the plasma are a serious problem for ^{28}Si ($^{12}\text{C}^{16}\text{O}$, $^{14}\text{N}_2$), ^{39}K (^{38}ArH), ^{40}Ca (unresolvable from ^{40}Ar), ^{52}Cr ($^{40}\text{Ar}^{12}\text{C}$), and ^{56}Fe ($^{40}\text{Ar}^{16}\text{O}$), and these elements were monitored at a minor isotope with a more favorable ratio of analyte peak to molecular isobaric interference. There are also atomic isobaric interferences originating from the sample (^{48}Ca , ^{58}Fe) that affect ^{48}Ti and ^{58}Ni , so these elements were monitored at minor isotopes. The extent of molecular isobaric interferences from the plasma was monitored with a gas blank (Table 2). All peaks were acquired in low mass resolution ($M/\Delta M = 400$) by repeatedly sweeping the mass spectrometer in peak-jumping mode (EScan). In low mass resolution, molecular isobaric interferences could not be spectrally resolved from analyte peaks but had to be swamped by the signal. All molecular isobaric interferences, except for $^{38}\text{Ar}^1\text{H}$, could have been spectrally resolved at higher mass resolving power on the Element XR, but the beam intensity needed to swamp the interference on ^{39}K also swamped the interferences on the other peaks.

Some measurements were initially performed using the “Triple” mode option of the Element XR, where the instrument assigns the detector mode in live time. However, a software glitch occurred for some peaks where the assignment was not properly made, and no data were recorded. This glitch affected K and P abundances in BCR-2G (Table 3). Peaks for ^{23}Na and ^{27}Al in some samples reached intensities ($>10^8$ cps) sufficient to place on the Faraday cup and switch-over issues affected the data. After this the detector mode was assigned as Analog mode for all elements even though some of the peaks exceeded the nominal range for the Analog mode.

Peak intensities were stripped of background intensities measured with the laser off, and then converted to oxide concentration ratios with respect to silica using relative sensitivity factors⁷ defined as,

$$RSF = \frac{C_i/C_{\text{SiO}_2}}{I_i/I_{29\text{Si}}} \quad (\text{eqn. 1})$$

where C_i is the concentration of element or oxide i , and I_i is the intensity of the peak monitored for that element or oxide. Relative sensitivity factors were obtained by averaging duplicate

Table 2 List of peaks, interferences, typical background and sample intensities, and detection limits (% m/m, except Cr and Ni in $\mu\text{g/g}$)

	Isotope	Isobaric interferences	blank intensity (kcps)	BHVO-2G intensity (kcps)	Average detection limit
SiO ₂	²⁹ Si	¹³ C ¹⁶ O, ¹⁵ N ¹⁴ N	250	28,900	0.02
TiO ₂	⁴⁷ Ti	—	20	11,900	0.0003
Al ₂ O ₃	²⁷ Al	—	410	427,000	0.002
FeO _T	⁵⁷ Fe	⁴⁰ Ar ¹⁶ O ¹ H	120	19,500	0.006
MnO	⁵⁵ Mn	⁴⁰ Ar ¹⁴ N ¹ H, ³⁸ Ar ¹⁶ O ¹ H	60	15,200	0.00002
MgO	²⁵ Mg	—	16	23,600	0.0007
CaO	⁴⁴ Ca	¹² C ¹⁶ O ₂	500	19,980	0.05
Na ₂ O	²³ Na	—	1,400	116,000	0.01
K ₂ O	³⁹ K	³⁸ Ar ¹ H	2,200	54,000	0.002
P ₂ O ₅	³¹ P	—	36	680	0.0002
Cr	⁵³ Cr	⁴⁰ Ar ¹³ C	3	259	0.1
Ni	⁶⁰ Ni	—	65	303	1.5

Table 3 Replicate analyses of USGS fused basalt (silicate) reference materials BCR-2G and BHVO-2G by laser ablation ICP-MS (this study) compared with GeoReM preferred values.^{13–15} Units are % m/m, except Cr and Ni in µg/g

	BCR-2G							BHVO-2G				
	LA-ICP-MS				Average	RSD 1σ	GeoReM ¹⁴	LA-ICP-MS		Average	GeoReM ¹⁵	
	(1)	(2)	(3)	(4)				(1)	(2)			
SiO ₂	55.03	54.88	55.26	55.15	55.08	<1%	54.4 ± 4	50.42	49.86	50.14	49.3 ± 1	
TiO ₂	2.29	2.31	2.33	2.34	2.32	1%	2.27 ± 4	2.90	2.87	2.88	2.79 ± 2	
Al ₂ O ₃	14.13	14.56	13.41	13.48	13.89	4%	13.4 ± 4	13.23	13.23	13.23	13.6 ± 1	
FeO _T	12.24	12.30	12.50	12.58	12.41	1%	12.4 ± 3	11.18	11.40	11.29	11.3 ± 1	
MnO	0.198	0.203	0.202	0.199	0.201	1%	0.19 ± 1	0.172	0.174	0.173	0.17 ± 3	
MgO	3.64	3.59	3.57	3.54	3.58	1%	3.56 ± 9	7.35	7.59	7.47	7.13 ± 2	
CaO	7.21	7.22	7.14	7.13	7.18	1%	7.06 ± 11	11.67	11.73	11.70	11.4 ± 1	
Na ₂ O	3.31	3.30	3.50	3.49	3.40	3%	3.23 ± 7	2.34	2.42	2.38	2.4 ± 1	
K ₂ O	1.64	1.63	1.74	1.76	1.69	4%	1.74 ± 4	0.50	0.48	0.49	0.51 ± 2	
P ₂ O ₅	0.32	—	0.34	0.34	0.33	4%	0.37 ± 1	0.25	0.25	0.25	0.29 ± 2	
Cr	19	—	17	16	17	9%	17 ± 2	334	334	334	293 ± 12	
Ni	5	5	7	6	6	21%	13 ± 2	109	108	108	116 ± 7	

analyses of the MPI-DING glass reference materials:⁶ GOR128-G, ML3B-G, KL2-G, T1-G, StHs6/80-G, and ATHO-G, which represent nearly the full range of major element composition (e.g., SiO₂ = 44–75%) occurring in natural silicate glasses. Intensity ratios obtained for some elements from some of these reference materials had blank corrections of greater than 10%, and were then excluded from the calculation of the average RSF. The USGS glass reference materials^{11,12} BHVO-2G and BCR-2G were run as independent controls.

Application of the RSFs results in a set of oxide or elemental (e.g., Cr) concentration ratios relative to SiO₂. The silica content is determined from eqn. 2 as,

$$SiO_2 = \frac{100}{\sum \frac{x_i}{SiO_2}} \quad (\text{eqn. 2})$$

where x_i is an oxide, including SiO₂. For each glass, oxide ratios to silica were converted to oxide concentrations by multiplying by the silica content determined from eqn. 2. Accordingly, the oxide totals are required to equal 100%. Detection limits for each spot size were calculated from intensity ratios to silica of 3× the standard deviation of a set of three blanks taken with the laser off. The detection limits scale inversely with the size of the signal, and decrease with increasing spot size used. A typical set of detection limits obtained is given in Table 2.

Results and discussion

Precision and accuracy of USGS reference materials

Major element analyses (including Cr and Ni) of the USGS reference materials BCR-2G and BHVO-2G are given in Table 3. The precision of the LA-ICP-MS technique for major element analysis can be assessed by examining the reproducibility of multiple analyses of the USGS glass reference materials BHVO-2G and BCR-2G, which were run together with the MPI-DING glasses, but not used in calculations of the RSFs. For the four replicate measurements of BCR-2G, the precision is about 1%, except for Al₂O₃, Na₂O, K₂O, and P₂O₅, which have reproducibilities of 3–4%, and the trace elements Ni (6 µg/g, RSD = 21%) and Cr (16 µg/g, RSD = 9%), which are at µg/g-level

concentrations in BCR-2G. The accuracy of the data can be assessed from Figure 3, where the percentage deviation of the major element compositions determined in this work from the preferred values^{13–15} (Table S1†) are shown. The deviations are a few percent, except for some Al₂O₃ and Na₂O data (see below), and P₂O₅ which is systematically low by 10–15%. The Cr abundances in both reference materials, and the Ni abundances in BHVO-2G, are accurate within their precision of 10–20%. The Ni abundances of BCR-2G are a factor of two lower than the preferred values,¹⁴ but the technique used in the present study was not optimized for low-level Ni as ⁶⁰Ni was determined in analog mode.

A further indication of the accuracy is the precision with which RSFs can be determined for the MPI-DING glasses, relative to the values with which those glasses are known. The relative uncertainties obtained from GeoReM for the MPI-DING and USGS glass reference materials are given in Table 4. The relative standard deviations of the RSFs obtained in the analytical session used to determine the standard values in Table 3 are also given in Table 4. Since the uncertainties in the MPI-DING reference materials contribute to the RSDs of the RSFs obtained,

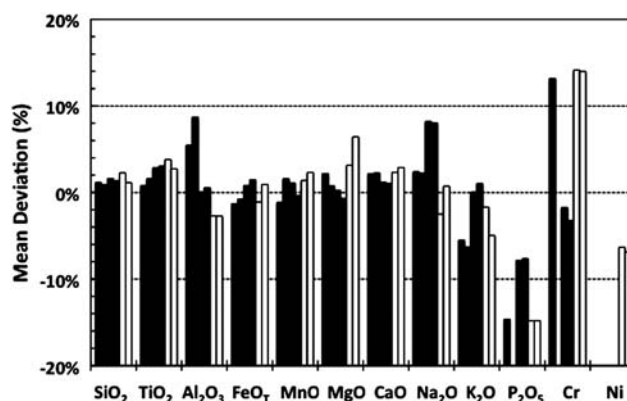


Fig. 3 Histogram showing mean deviations (%) of replicate LA-ICP-MS analyses of USGS standard glasses BCR-2G (black bars) and BHVO-2G (white bars) from the GeoReM preferred values.^{13–15}

Table 4 Uncertainties assigned by GeoReM^{13–15,29} for MPI-DING and USGS glass reference materials, expressed here as percent relative deviation. Italicized values for MPI-DING reference materials were not used in calibration

	GOR128-G	KL2-G	ML3B-G	T1-G	StHs6/80-G	ATHO-G	Average RSFs	BCR-2G	BHVO-2G ^a
SiO ₂	1%	1%	1%	1%	1%	1%	—	1%	0%
TiO ₂	4%	4%	4%	2%	3%	6%	3%	2%	1%
Al ₂ O ₃	2%	2%	1%	1%	1%	2%	2%	3%	1%
FeO _T	1%	1%	1%	1%	2%	3%	2%	2%	1%
MnO	5%	5%	5%	5%	5%	5%	4%	5%	18%
MgO	1%	1%	1%	1%	2%	10%	2%	3%	0%
CaO	2%	2%	1%	1%	2%	2%	4%	2%	1%
Na ₂ O	5%	3%	3%	3%	3%	8%	3%	2%	4%
K ₂ O	14%	2%	1%	2%	2%	3%	14%	2%	4%
P ₂ O ₅	20%	11%	11%	15%	11%	16%	9%	3%	7%
Cr	8%	9%	13%	10%	20%	23%	17%	12%	4%
Ni	6%	4%	8%	12%	16%	38%	19%	15%	6%

^a Values for BHVO-2G are “information values”.¹⁵

the comparison is interesting. The uncertainty of SiO₂, 1%, is compounded with the RSDs of the other elements, since the RSFs are ratios to SiO₂. Most of the RSFs exhibit RSDs that are 2–4%, which compare favorably with the uncertainties of the MPI-DING glasses. The exceptions are all in the minor or trace elements, including P₂O₅, where the RSD is better than the uncertainties, and K₂O, Cr and Ni, where the RSDs are worse than the uncertainties of the reference materials used in the calibration. To a large degree, the uncertainties of our laser ablation major element method are limited by the accuracy to which the reference materials are known.

Precise determination of the MnO abundance (± 1 –2%) is a challenge for many techniques, but MnO in silicate minerals is a major focus of our geochemical program.^{16–18} The glasses analyzed in this study were prepared by melting whole-rock powders (WR), the abundances of which have been better characterized than those of the glasses alone. Table 5 compares MnO abundances for the BHVO-2 and BCR-2 whole-rock powders (WR) with those of the glasses. Our laser ablation ICP-MS method obtained MnO abundances of BCR-2G and BHVO-2G that are within 1–2% of the WR value determined by precise solution nebulization techniques.^{17,18} This is unexpected, since the MPI-DING glasses used in the calibration have relative uncertainties of $\pm 5\%$ on their MnO abundances, and RSDs of their RSFs of 4% (e.g., Table 4). Nonetheless, Table 3 shows that the precision and accuracy of the LA-ICP-MS major element

analysis is 1–2% for the determination of MnO at levels typical in natural silicate glasses, an exercise performed earlier using a 266 nm laser ablation system.¹⁷

Volume-averaged analysis of heterogeneous silicate mixtures

The application of LA-ICP-MS to volume-averaged analysis of the experimental partial melt charge (A682) shown in Figure 1 yields a large amount of compositional information. In Figure 4, compositional data are shown as individual mass scans of the mass spectrum collected as the sample surface was scanned in line mode beneath the UP193FX at 5–10 $\mu\text{m/s}$. Each LA-ICP-MS data point represents a mere 50 milliseconds of peak-top integration. Also shown are EMP analyses, where each EMP data point represents 30 seconds (15 seconds for Na₂O) of peak+background integration. The volume sampled by each EMP probe spot is $\sim 1 \mu\text{m}^3$, while the volume sampled by each LA-ICP-MS data point is $\sim 800 \mu\text{m}^3$ (20 μm spot) to $\sim 3200 \mu\text{m}^3$ (50 μm spot). Although 5 LA-ICP-MS tracks were taken in total on A682, to limit cluttering results from only three tracks are shown in Figure 4. These include a 20 μm beam spot scanned at 5 $\mu\text{m/s}$, and a 50 μm beam spot scanned at 10 $\mu\text{m/s}$, over the quenched melt phase, and a 50 μm beam spot scanned at 10 $\mu\text{m/s}$ over the residue (see track locations marked on Figure 1). The composition of the residual minerals determined by EMP provides some interesting perspectives on the technique. The residual phases are not homogeneously distributed in A682, but are concentrated in zones that can be observed in the back-scattered electron image (Figure 1) by their varying shades of gray. The region near the quenched melt is composed chiefly of olivine and orthopyroxene, followed by an olivine-clinopyroxene layer, followed by garnet-rich residue at the end farthest from the melt phase, and all regions contain some trapped melt. The individual minerals form small crystals, 10–20 μm in diameter, the compositions of which were determined by EMP and are shown in Figure 4. It is evident from plots of MgO vs. SiO₂, CaO, and FeO_T (Figure 4) that the 50 μm laser track sampled a mixture of olivine and clinopyroxene with some trapped melt. Elemental abundances that are dominated by the crystalline minerals form excellent correlations in oxide vs. MgO plots (Figure 4).

Table 5 Comparison of MnO abundances determined in USGS reference materials by laser ablation and solution nebulization methods

Sample	MnO (% m/m)	Reference
BHVO-2 (WR)	0.171	Huang <i>et al.</i> (2007) ¹⁸
BHVO-2 (WR)	0.169	Qin <i>et al.</i> (2008) ¹⁷
BHVO-2 (WR)	0.170 \pm 5	GeoReM ²⁸
BHVO-2 (WR)	0.167 \pm 5	USGS certified value ¹²
BHVO-2G	0.173	This study
BHVO-2G	0.170 \pm 30	GeoReM ¹⁵
BCR-2 (WR)	0.201	Qin <i>et al.</i> (2008) ¹⁷
BCR-2 (WR)	0.20 \pm 1	GeoReM ²⁸
BCR-2 (WR)	0.196 \pm 8	USGS certified value ¹¹
BCR-2G	0.201 \pm 2	This study
BCR-2G	0.19 \pm 1	GeoReM ¹⁴

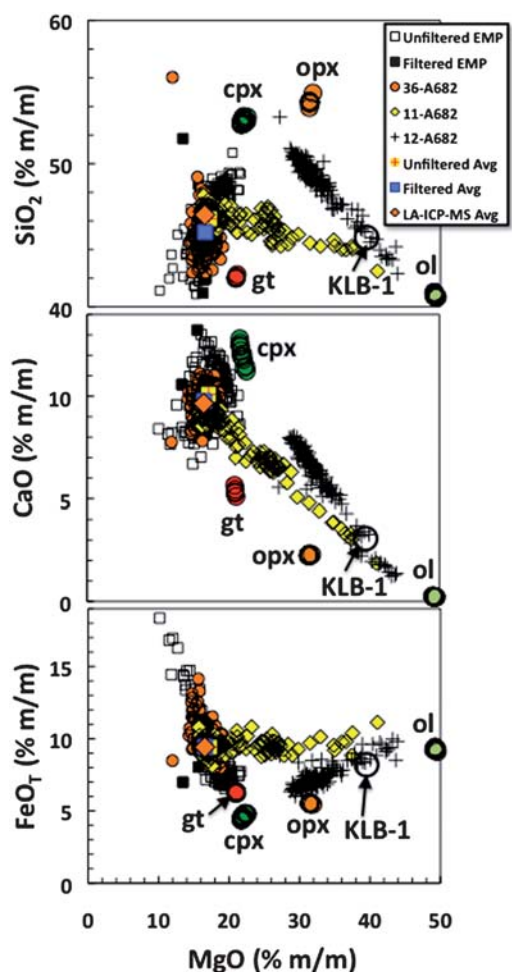


Fig. 4 Plots of SiO₂, CaO, and FeO_T vs. MgO plots for sample A682. Mineral compositions (ol, opx, cpx, gt) determined by EMP, and quenched melt compositions determined by EMP and LA-ICP-MS, are shown. Also featured is a track through the residue that defines a clinopyroxene (cpx)-olivine (ol) mixing line. The position of the LA-ICP-MS tracks is shown in Figure 1. Filtered EMP data (n = 28) are a subset of the unfiltered EMP data (n = 160) that pass the filtering criteria applied. Note that the raw EMP average is biased towards cpx, while the average of the 20 μm LA-ICP-MS measurements are biased away from cpx. Abbreviations: olivine (ol), clinopyroxene (cpx), orthopyroxene (opx), garnet (gt), bulk-starting composition (KLB-1).

The precision of a single scan (σ) was estimated from the correlations as,

$$\sigma = \sqrt{\frac{\sum (y_i - y_c)^2}{\sum y_i^2}} \quad (\text{eqn. 3})$$

where, y_i is the component of interest (e.g., SiO₂, CaO, or FeO_T), and y_c is the value obtained from a linear regression between MgO and one of these components. The precision of a single scan is excellent, being about 1% for SiO₂, and 3–5% for Al₂O₃, FeO_T, MnO, CaO, Na₂O and Cr. Elemental abundances that are dominated by the quench melt (TiO₂, K₂O) do not exhibit simple mixing lines between olivine and clinopyroxene and exhibit reproducibilities of 10–20% that are dominated by sample heterogeneity. Based on representative intensities given in Table 2, it is worth noting here that each scan had $\sim 10^5$ – 10^7

counts for all elements, except P, which had 10-fold smaller total counts.

The primary goal of this study was to obtain volume-averaged analyses of the heterogeneous quenched melt. The EMP unfiltered analyses produce a broad scatter which trend towards the clinopyroxene composition, one of the phases forming the quenched matter of crystals and glass evident in Figure 2. The individual scans from the 20 μm track plot along the EMP spots, but exhibit a smaller dispersion (Figure 4). In plots of SiO₂, CaO, and FeO_T vs. MgO, the 20 μm LA-ICP-MS data exhibit a bias away from the clinopyroxene composition, opposite that of the EMP spots, indicating that they are preferentially sampling a phase that may have been under-sampled by the EMP analyses due to selective removal by plucking during polishing. The individual scans of the 50 μm LA-ICP-MS data plot along an olivine-melt mixing line in Figure 4, indicating beam overlap with olivine crystals adjacent to the quenched melt region. However, the 50 μm individual scans provide better averaging of the melt phase than either the 20 μm LA-ICP-MS data or the EMP spots. Because of the overlap on olivine, the MgO range had to be constrained from the 20 μm beam spot track. Once the MgO was known, the 50 μm beam spot track data were filtered to exclude the high-MgO data points, and an average of the remaining data was used to derive the composition of the quenched melt (Table 6). For the 20 μm track, a straight average of the data sufficed. Table 6 compares the average quenched phase composition for A682 obtained by the four different

Table 6 Average quench melt composition (% m/m, except Cr in μg/g) for A682 derived from four different approaches (see text for discussion), together with their RSDs. The number of data points in the average is given by n, and the volume sampled during analysis is also provided (in μm³)

	LA-ICP-MS 20 μm	LA-ICP-MS 50 μm	Raw EMP	Filtered EMP
n	196	65	158	26
Vol. (μm ³)	152,000	211,000 ^a	158	26
SiO ₂	45.32	46.42	46.15	45.21
TiO ₂	2.38	2.35	2.04	2.25
Al ₂ O ₃	12.75	12.62	12.18	13.20
FeO _T	9.93	9.42	9.42	9.44
MnO	0.168	0.159	0.15	0.15
MgO	16.76	16.56	17.24	16.63
CaO	9.68	9.65	10.10	9.77
Na ₂ O	2.40	2.17	2.06	2.51
K ₂ O	0.564	0.629	0.49	0.70
P ₂ O ₅	0.028	0.036	—	—
Cr	1170	1128	1230	978
	RSD %	RSD %	RSD %	RSD %
SiO ₂	3%	1%	5%	5%
TiO ₂	8%	4%	25%	19%
Al ₂ O ₃	4%	3%	13%	14%
FeO _T	10%	4%	25%	7%
MnO	6%	3%	23%	22%
MgO	6%	3%	12%	5%
CaO	6%	3%	13%	12%
Na ₂ O	15%	5%	45%	25%
K ₂ O	26%	8%	117%	65%
P ₂ O ₅	34%	36%	—	—
Cr	14%	5%	44%	39%

^a The volume of the portion of track that was used in the melt composition calculation.

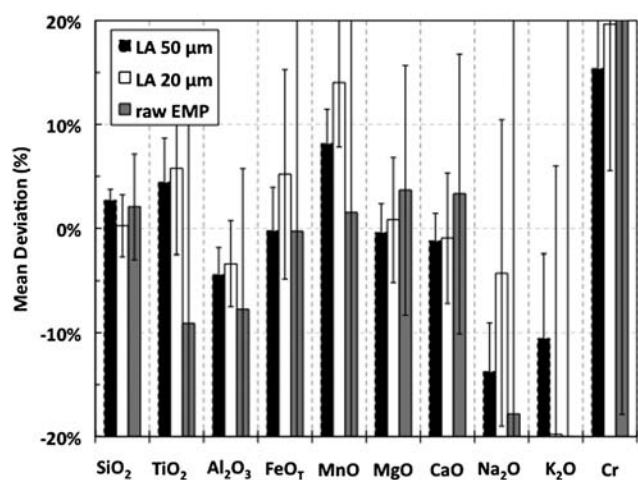


Fig. 5 Comparison of three different estimates of melt compositions for A682, including averages of the 20 μm and the 50 μm LA-ICP-MS tracks and the average of raw EMP analyses, plotted as percent deviations from the filtered EMP average. The RSDs are shown as error bars, and do not take into account the RSDs of the filtered EMP average.

approaches: average 20 μm beam spot, average 50 μm beam spot, average of EMP spots, and average of filtered EMP spots. These compositions are fairly close to one another in Figure 4, where the 20 μm beam spot average is not shown. Table 6 also shows the estimated analytical volume sampled by each compositional average, where the volume for the 50 μm track was calculated only with those data points that were used in the compositional averaging (total track volume was 650,000 μm^3).

In Figure 5, the four estimates of the melt composition are compared as deviations from the filtered EMP line average, together with their RSDs. The agreement of the 50 μm and 20 μm LA-ICP-MS data with the filtered EMP average is better than 5% for SiO_2 , TiO_2 , FeO_T , MgO and CaO . The filtered EMP average over-estimates Al_2O_3 , Na_2O , and K_2O , relative to the LA-ICP-MS data, and underestimates MnO and Cr . This is partly due to the smaller number of data points remaining in the filtered EMP average ($n = 28$), relative to either the raw EMP averages ($n = 160$) or the LA-ICP-MS data (Table 6), which must not adequately represent the spectrum of heterogeneity within the quenched melt phase (Figure 4). Further, the EMP data systematically underestimate MnO by $\sim 10\%$, so the LA-ICP-MS data are more accurate here, as seen from Table 5. The RSDs of the 50 μm LA-ICP-MS data are 1–5% for all elements, except K_2O (8%) and P_2O_5 . Phosphorus was not added to the experimental charge, but was incidentally present as an impurity. Given the analytical limits imposed by heterogeneity of the quenched melt, the LA-ICP-MS method provides an alternative means of obtaining the melt composition that is generally more precise, and for some minor elements potentially more accurate, than EMP techniques. This study has demonstrated that the usual bias against using LA-ICP-MS as a major element technique is no longer justified.

Broader applicability of the LA-ICP-MS method

Although we have used a sector field ICP-MS instrument and a short wavelength laser (193 nm) in this study, we evaluate the

factors contributing to successful analysis here and consider the possible use of other instruments for this measurement. In general, sector-field instruments have an advantage in sensitivity and particularly in mass resolving power over quadrupole ICP-MS instruments.¹ However, the measurements described here were more challenged by beams that were too intense than by requirements for better sensitivity. Also, all measurements were performed in low resolution mode and so could be duplicated by quadrupole ICP-MS. The key factors in our success have been recent developments involving a better understanding of the sources of non-stoichiometric ablation in silicate glasses (fractionation)⁸ and the availability of better reference materials than previously available.^{6,8}

A recent study of fractionation of alkali elements during ablation of silicates, including BCR-2G, with a 213 nm laser found significant non-stoichiometric ablation effects in all glass samples studied,¹⁹ which have not proven to be limitations in either this study with a 193 nm laser or in our previous work with a 213 nm laser.⁸ For example, Na_2O and K_2O abundances in BCR-2G analyzed in the present study (Table 3) agree within 5% with preferred values^{13,14} for these glass reference materials (Figure 3). There are several key strategies that minimize the effects of non-stoichiometric ablation,⁸ most importantly avoiding formation of deep craters by moving the laser track along a line scan.⁴

The laser wavelength has a smaller impact²⁰ on success. We have previously used a 213 nm laser to much the same effect, but limited in the number of major elements.^{7,8} The shorter pulse-width of femto-second lasers may offer significant improvements in stability^{21,22} over nano-second lasers.¹

The applicability of this method to individual spots, and to spot sizes similar to those used by EMP ($\sim 1 \mu\text{m}$), has yet to be evaluated. The current measurements were not limited by sensitivity. Even when the limit of sensitivity is reached in low mass resolution, the Element XR can improve its performance by resorting to higher mass resolving power with K_2O presenting challenges at smaller spot sizes.

We expect that this method should find wide application in LA-ICP-MS labs employing a range of lasers and either sector-field or quadrupole ICP-MS. This method should be particularly important in geochemical^{23,24} and archeometric applications, but forensic finger-printing of float glass²⁵ may also benefit from improved determinations of the major constituents of glasses.

Conclusions

We demonstrate that with appropriate standardization LA-ICP-MS provides both precise and accurate major element compositions for silicates. Elemental analysis of the USGS glass reference materials BCR-2G and BHVO-2G yield precise abundances: $\sim 1\%$ for major constituents (e.g., SiO_2 , TiO_2 , FeO_T , MnO , MgO , CaO), 3–4% for Al_2O_3 and minor constituents (Na_2O , K_2O , P_2O_5), and 10–20% for trace elements (Ni, Cr). Using the MPI-DING glass reference materials for calibration, we obtained agreement with preferred values of the USGS glass reference materials of better than 5% for all major constituents, except Al_2O_3 , Na_2O , and P_2O_5 , and better than 10–20% for trace constituents. The analysis of ^{23}Na and ^{27}Al , the two most intense peaks, for the USGS reference materials was affected by detector

issues unique to the Element XR, and avoidable in future measurements. Abundances for P₂O₅ were systematically lower, which remains to be resolved.

Application of this method to the volume-averaged analysis of a heterogeneous silicate charge (A682) formed by quenching of an experimental partial melt showed that single scans (50 milliseconds/peak) yielded precision within 5% for most major constituents. Mixtures of olivine and clinopyroxene analyzed by LA-ICP-MS produced trends that intersected the compositions of these minerals as determined by EMP. Comparison of EMP averages and LA-ICP-MS averages showed that the LA-ICP-MS averages are more effective at recovering bulk composition of the quenched melt. The analysis of some minor elements, particularly MnO, was more precise, and the MnO abundances demonstrably more accurate (1–2%) by LA-ICP-MS.

The accurate analysis of both Na₂O and K₂O in BCR-2G indicates that the methodology employed here successfully controlled non-stoichiometric ablation (fractionation) artifacts reported in other studies.¹⁹ The key features of success were appropriate standardization with reference materials higher in iron than NIST glasses and avoidance of deep craters in favor of line scans, strategies we have previously demonstrated with 266 nm and 213 nm laser systems.^{4,8}

Because the methodology employed for major element analysis did not depend on any of the unique features of sector-field ICP-MS, extension of this method to quadrupole ICP-MS, and to other laser systems, is entirely feasible.

Acknowledgements

We thank two anonymous referees for their constructive comments which contributed greatly to the improvement in presentation of this article. This research was partially supported by the NASA Cosmochemistry program (NNX09AG87G, Humayun) and by the NSF Petrology and Geochemistry program (EAR 0609967, Hirschmann).

Notes and references

- 1 J. Pisonero, B. Fernandez and D. Günther, *J. Anal. At. Spectrom.*, 2009, **24**, 1145–1160.
- 2 C. C. Garcia, H. Lindner and K. Niemax, *J. Anal. At. Spectrom.*, 2009, **24**, 1–116.
- 3 K. P. Jochum, B. Stoll, K. Herwig and M. Willbold, *J. Anal. At. Spectrom.*, 2007, **22**, 112–121.
- 4 A. J. Campbell and M. Humayun, *Anal. Chem.*, 1999, **71**, 939–946.

- 5 A. J. Campbell, M. Humayun and M. K. Weisberg, *Geochim. Cosmochim. Acta*, 2002, **66**, 647–660.
- 6 K. P. Jochum, B. Stoll, K. Herwig, M. Willbold, A. W. Hofmann, M. Amini, S. Aarburg, W. Abouchami, E. Hellebrand, B. Mocek, I. Raczek, A. Stracke, O. Alard, C. Bouman, S. Becker, M. Dücking, H. Bratz, R. Klemm, D. de Bruin, D. Canil, D. Cornell, C. J. de Hoog, C. Dalpe, L. Danyushevsky, A. Eisenhauer, W. R. Premo, W. D. D. Sun, M. Tiepolo, R. Vannucci, T. Vennemann, D. Wayne and J. D. Woodhead, *Geochem., Geophys., Geosyst.*, 2006, **7**, 1–44.
- 7 M. Humayun, S. B. Simon and L. Grossman, *Geochim. Cosmochim. Acta*, 2007, **71**, 4609–4627.
- 8 M. Gaboardi and M. Humayun, *J. Anal. At. Spectrom.*, 2009, **24**, 1188–1197.
- 9 F. A. Davis, J. A. Tangeman, T. J. Tenner and M. M. Hirschmann, *Am. Mineral.*, 2009, **94**, 176–180.
- 10 M. J. Toplis, *Contrib. Mineral. Petrol.*, 2005, **149**, 22–39.
- 11 S. A. Wilson, *United States Geological Survey, Certificate of Analysis, Basalt, Columbia River, BCR-2*, 12/2008, (http://minerals.cr.usgs.gov/geo_chem_stand/basaltbcr2.pdf).
- 12 S. A. Wilson, *United States Geological Survey, Certificate of Analysis, Basalt, Hawaiian Volcanic Observatory, BHVO-2*, 12/2008, (http://minerals.cr.usgs.gov/geo_chem_stand/basaltbhvo2.pdf).
- 13 K. P. Jochum and U. Nohl, *Chem. Geol.*, 2008, **253**, 50–53.
- 14 K. P. Jochum and F. Nehring, *GeoReM, BCR-2G GeoReM preferred values*, 7/2008, (<http://georem.mpch-mainz.gwdg.de>).
- 15 K. P. Jochum and F. Nehring, *GeoReM, BHVO-2G GeoReM preferred values*, 7/2008, (<http://georem.mpch-mainz.gwdg.de>).
- 16 M. Humayun, L. Qin and M. D. Norman, *Science*, 2004, **306**, 91–94.
- 17 L. Qin and M. Humayun, *Geochim. Cosmochim. Acta*, 2008, **72**, 1660–1677.
- 18 S. Huang, M. Humayun and F. A. Frey, *Geochim. Cosmochim. Acta*, 2007, **71**, 4557–4569.
- 19 J. Mikova, J. Kosler, H. P. Longerich, M. Wiedenbeck and J. Hanchar, *J. Anal. At. Spectrom.*, 2009, **24**, 1244–1252.
- 20 J. Gonzalez, X. L. Mao, J. Roy, S. S. Mao and R. E. Russo, *J. Anal. At. Spectrom.*, 2002, **17**, 1108–1113.
- 21 R. Freydier, F. Candaudap, F. Poitrasson, A. Arbouet, B. Chatel and B. Dupre, *J. Anal. At. Spectrom.*, 2008, **23**, 702–710.
- 22 Q. Bian, C. C. Garcia, J. Koch and K. Niemax, *J. Anal. At. Spectrom.*, 2006, **21**, 187–191.
- 23 Z. S. Yu, M. D. Norman and P. Robinson, *Geostand. Geoanal. Res.*, 2003, **27**, 67–89.
- 24 M. D. Norman, W. L. Griffin, N. J. Pearson, M. O. Garcia and S. Y. O'Reilly, *J. Anal. At. Spectrom.*, 1998, **13**, 477–482.
- 25 S. Berends-Montero, W. Wiarda, P. de Joode and G. van der Peijl, *J. Anal. At. Spectrom.*, 2006, **21**, 1185–1193.
- 26 J. V. Smith and P. H. Ribbe, *J. Geol.*, 1966, **74**, 197–216.
- 27 E. Jarosewich, J. A. Nelen and J. A. Norberg, *Geostand. Geoanal. Res.*, 1980, **4**, 43–47.
- 28 K. P. Jochum and F. Nehring, *GeoReM, BCR-2, BHVO-2, GeoReM preferred values*, 12/2008, (<http://georem.mpch-mainz.gwdg.de>).
- 29 K. P. Jochum and J. Herwig, *GeoReM, MPI-DING glasses, GeoReM preferred values*, 12/2008, (<http://georem.mpch-mainz.gwdg.de>).
- 30 M. Guillion, K. Hametner, E. Reusser, S. A. Wilson and D. Gunther, *Geostand. Geoanal. Res.*, 2005, **29**, 315–331.
- 31 Y. Liu, Z. Hu, S. Gao, D. Gunther, J. Xu, C. Gao and H. Chen, *Chem. Geol.*, 2008, **257**, 34–43.